A Bayesian PASL-MRI perfusion estimation algorithm with spatio-temporal edge preserving priors

Miguel L. Rodrigues, *Biomedical Engineering, Instituto Superior Técnico*

***Abstract*—*Arterial Spin Labeling* (ASL) is a non-invasive technique for generating perfusion images of the brain. Since it does not require the use of an artificial tracer, it has been significantly gaining recognition as a method for obtaining perfusion parameters. Following an alternating labeling/control acquisition sequence, the minor magnetization difference between labeled and non-labeled images is detected by performing image subtraction. Due to the intrinsically low *Signal to Noise Ratio* (SNR), label/control acquisitions must be repeated a number of times and signal averaging is then performed in order to detect the small perfusion dependent difference signal. In this work, a novel ASL data analysis approach is proposed, in which the averaging procedure is not done explicitly. The magnetization difference estimation problem is formulated in a Bayesian framework, where spatio-temporal priors are used to deal with the ill-posed nature of the estimation task, hence enabling shorter acquisition times, without compromising the estimation quality. The *a priori* assumption that no drastic signal variations are expected along the same tissue, except at the organs boundaries, is imposed by the priors. To evaluate the performance of the proposed algorithm, the results obtained using synthetic data were compared against the two most common subtraction methods used to process ASL data, pair-wise and surround subtraction. The results were very encouraging, as greater SNR was achieved and the overall mean-squared error was highly reduced. The proposed algorithm was then applied to a real data-set, also obtaining satisfactory results.**

***Index Terms*—arterial spin labeling, bayesian approach, perfusion, magnetization, spatio-temporal priors**

I. Introduction

Cerebral Blood Flow (CBF) is a measure of the volume of blood passing through a point in the brain circulation per unit of time and, in a healthy individual, alterations in neural activity lead to changes in local CBF[1]. If the volume of the tissue is taken into account, the *perfusion* can also be measured, as the CBF per unit volume of tissue. In fact, perfusion is the process by which the nutrients in the blood stream are delivered to the tissues through the capillary bed. It is a parameter that provides very useful information about the condition of a certain organ. There are many techniques to assess the previous mentioned hemodynamic parameters, and this work is focused on a technique whose potential is widely recognized: Arterial Spin Labeling (ASL).

In ASL, the blood passing through a determined region (upstream from the region of interest) is labeled with an inversion pulse, and after a certain time interval (TI), the blood reaches the region of interest and an image is acquired. If a control image, where no labeling was performed, is subtracted from the labeled acquisition, the resulting image has a small magnetization difference caused by the exchange of labeled water molecules from the blood to the surrounding tissue, which is an indicator of CBF. Since the magnetization difference is very small, a set of label-control acquisitions has to be performed to obtain an image with sufficient SNR.

This work was supported by project FCT (ISR/IST plurianual funding) through the PIDDAC Program funds.

Institute for Systems and Robotics and Bioengineering Department from Instituto Superior Técnico / Technical University of Lisbon

II. Arterial Spin labeling

In the last two decades, Arterial Spin Labeling Magnetic Resonance Imaging (ASL MRI) perfusion technology brought great innovation into human brain function and perfusion imaging.

As previously mentioned, ASL is a non-invasive technique that allows the quantification of brain perfusion, which is a measure of the rate at which nutrients and oxygen are delivered by the blood flow to the tissues in the capillary bed and it is considered to be one of the most fundamental physiological parameters[2], [3]. For instance, perfusion disorders account for most of the leading causes of medical disability and mortality. Furthermore, ASL can provide perfusion maps that can be of great use when interpreting several conditions, such as tumors, acute stroke, chronic cerebrovascular disease, epilepsy and several degenerative diseases[4].

The ASL method consists on the labeling of the water protons present in the blood of the vessels that supply the region to be imaged. After a certain period of time, named *post labeling delay* (PLD), the labeled blood reaches the region to be imaged and then an image is acquired. In order to acquire a control image, the procedure is repeated without the labeling of the blood. It is the subtraction of the control and labeled image that allows the remotion of static tissue signal, hence allowing the creation of the perfusion image, since the remaining signal is expected to be a relative measure of the perfusion[5].

The signal difference is a very small fraction of the tissue signal (approximately 1-2%) and depends on many parameters, such as flow rate, T1 of the blood and tissue, and transit time for blood to travel from the labeling region to the imaging plane. To make sure that the SNR is sufficiently high to allow for a secure diagnostic review, several sequences of control-labeled images are acquired. A perfusion map can then be obtained by considering the *General Kinetic Model*[6].

The acquisition of an ASL image with an MRI pulse sequence has two independent components, *i.e.* preparation and acquisition components. The preparation component consists in the blood labeling with different magnetic states, in order to create the labeled and control images. The acquisition component refers to the data acquisition. ASL acquisition usually is performed using a fast acquisition method, such as Spiral or Echo Planar Imaging (EPI). The independence between the preparation and acquisition components has allowed researchers to choose the combination that best fits the experiment[5].

A. Continuous Arterial Spin Labeling

Continuous Arterial Spin Labeling (CASL) was the first ASL model to be proposed[7]. In this first approach, a continuous flow-driven adiabatic inversion scheme is used. The inversion of the arterial blood magnetization is performed using a continuous radio-frequency (RF) pulse (2-4 seconds) while applying a magnetic field gradient in the direction of the flow. A slow variation of the resonance frequency occurs in the moving arterial spins, resulting in their inversion, while the static tissues spin will only be saturated. The efficiency of the inversion is related to several factors, such as the mean velocity of the blood, angles of the vessels to the plane selected, RF amplitude, and gradient strength. The effectiveness of CASL is also affected by an effect occurring in long lasting inversion pulses, called the *Magnetization Transfer* (MT), which may lead to overestimated perfusion[8].

B. Pulsed Arterial Spin Labeling

The Pulsed modality of ASL was first proposed in 1994[9]. PASL uses a short RF pulse (typically between 5 to 20 ms) to invert a thick portion of spins in the proximal plane (10-15 centimeters distance) to the imaging region. Although the duration of the pulse is considerably smaller, the MT effects have to be considered as well.

The ease of implementation and reduced practical problems, when compared to CASL, have made PASL a popular choice for perfusion imaging. In fact, this is reflected in the wide range of sequences available today.

C. Pseudo-Continuous Arterial Spin Labeling - pCASL

Since CASL has small efficiency of labeling when compared to PASL, to face this disadvantage without raising the RF power deposition, a train of RF pulses in conjunction with a synchronous gradient field can be used to perform a flow-induced adiabatic inversion as in CASL.

Nowadays, pCASL can be performed in two different approaches. The first one is named *unbalanced pCASL*, where the gradients applied between two consecutive RF pulses are non-zero in labeling experiment and zero in control. The second approach, *balanced* pCASL, uses an identical gradient waveform with a residual moment for both labeling and control experiments. In both methods, RF polarity is alternated in the control sequence and constant in the labeled one[10]

The main advantages of these technique are an improvement of the balance labeling efficiency/image SNR, reduced MT effect and power deposition, when comparing with CASL[11].

D. Velocity Selective Arterial Spin Labeling

Velocity Selective ASL (VS-ASL), contrary to all methods previously depicted, does not invert the inflowing blood at a specific location. Instead, VS-ASL consists on saturating the blood moving at a velocity superior to a specified *cutoff* value, to achieve perfusion contrast. With VS-ASL, it is obtained a smaller and more uniform transit delay for the delivery of blood to the target tissue.

In the acquisition sequence, it is imposed the condition $V < V_c$, hence the resulting image includes labeled magnetization from spins that have decelerated during TI from above to below V_c, assuming that the velocities in the arterial tree are decreasing[12]. This is an important feature of VS-ASL since it functions as a filter for venous blood. In general, venous blood tends to accelerate, and as a large volume of venous blood is labeled, since it respects $V > V_c$ at the labeling instant, the condition $V < V_c$ will not be respected at the acquisition instant, thus leaving out the contribution of venous blood, that could compromise the validity of this method for obtaining CBF.

In Table I, an overall comparison of all ASL types is presented.

TABLE I
ASL TYPES - ADVANTAGES AND DISADVANTAGES

ASL Type	Advantages	Disadvantages
PASL	High labeling efficiency Lower SAR Improved transit time effects	Lower SNR Increased transit delay
CASL	Higher SNR than PASL Shorter transit delay	Lower labeling efficiency SAR Magnetization Transfer effects Continuous RF transmit hardware required
pCASL	Higher SNR than PASL Higher labeling efficiency than CASL Improved transit time effects	Higher SAR Limited clinical availability
VS-ASL	Ability to measure low CBF	lower SNR

ASL signal processing methods

As previously mentioned, in a typical ASL experiment a series of control and labeled images is acquired. These images are obtained in a alternate sequence, and a perfusion time series can be formed by subtracting labeled and control images [13]. Currently, there are three subtraction methods most commonly used [14]:

- Pair-wise subtraction
- Surround subtraction
- Sinc-interpolated subtraction

For a better understanding of the different types of subtractions about to be presented, let a set of acquisitions, expressed as an n length vector, be considered as:

$$[C_1, L_1, C_2, L_2, ..., C_{n/2}, L_{n/2}] \tag{1}$$

where the control images are identified as C_i and labeled images as L_i, with i varying from 1 to $n/2$. The value of the perfusion, P, can be extracted from this set of images.

Pair-wise subtraction: The Pair-wise subtraction, also known as *Simple Subtraction*, is the simplest method used. In this case, the perfusion is estimated by subtracting to each control image, the labeled image adjacent to it in the acquisition set. By performing this operation, it is expected for the remaining signal to be caused by the arterial labeling [14]. This can be mathematically represented as:

$$[P_1, P_2, ..., P_{n/2}] = [C_1 - L_1, C_2 - L_2, ..., C_{n/2} - L_{n/2}] \quad (2)$$

Ideally, the control and labeled images would be acquired at the same instant, but due to practical limitations of the ASL acquisition process, such as necessary transit time of blood from the region of labeling to the acquisition site (representing at least 2s between the acquisition of a labeled image and the next control), it is not feasible. During this period, signal fluctuations can occur, and these may not be attributed to the labeling effect. These signal fluctuations can be caused by random noise or systematic changes in the magnetization of the tissues as consequence of the pulse sequence, i.e., the BOLD effect.

Surround subtraction: In order to minimize the contribution from signal unrelated to perfusion, another method of performing the subtraction of control and labeled images was proposed in [15]. In the surround subtraction approach, each control image is subtracted by an average of the previous labeled image and the next labeled image, resulting in a difference signal insensitive to linear trends in the overall signal [15],

$$[P_1, ..., P_{n/2}] = [C_1 - L_1, C_2 - \frac{L_1 + L_2}{2}, ..., C_{n/2} - \frac{L_{(n/2)-1} + L_{n/2}}{2}] \quad (3)$$

High order signal variations, resulting from BOLD contrast will still be present in the difference signal, although with a small contribution.

Sinc-interpolated subtraction: First proposed in [14], the Sinc-interpolated subtraction attempts to remove the signal fluctuation effect caused by the time delay between the control and labeled images. Rather than a new approach, it can be considered as a complement of the Pair-wise subtraction. By doubling the temporal resolution of the labeled images vector through sinc interpolation, it is possible to re-sample at intermediate points in time, hence estimating the labeled images vector as if they had been acquired at the same time as the control images ($L_{1/2}$, $L_{3/2}$,...). Afterwards, by subtracting control and estimated labeled images, the perfusion vector is obtained.

$$[P_1, P_2, ..., P_{n/2}] = [C_1 - L_{1/2}, C_2 - L_{3/2}, ..., C_{n/2} - L_{n-1/2}] \quad (4)$$

The fractional numbers represent the projected time series at a point, one TR earlier in time.

The validity of this processing is based on the assumption that the perfusion signal does not suffer significant alterations in frequencies higher than the Nyquist frequency in the perfusion data. In fact, the lower the TR of data acquisition, the better the adaptability.

In this work, only two of the three signal processing methods will be used to assess and compare the results obtained by the proposed algorithm. These will be (a)*Pair-wise subtraction* and (b)*Surround-subtraction*.

III. Problem Formulation

Let $Y(t)$ be a sequence of L PASL images with $N \times M$ pixels. The observation model adopted in this paper is

$$Y(t) = F + D(t) + v(t)\Delta M + \mathbf{\Gamma}(t) \quad (5)$$

where $t \in \{1, 2, ..., L\}$ is an image index, $Y(t)$ is the t^{th} noisy image within the sequence, F is a time invariant $N \times M$ image describing the static magnetization of the tissues, $D(t)$ is a slow variant image describing the baseline fluctuations of the signal along time, called *Drift*, and ΔM is the magnetization variation in the tissues caused by the alternate inversion process occurring at each *inversion time* (TI). $\boldsymbol{v}(t)$ is a binary signal indicating the labeled periods related with the inversion process, as shown in Figure 1.

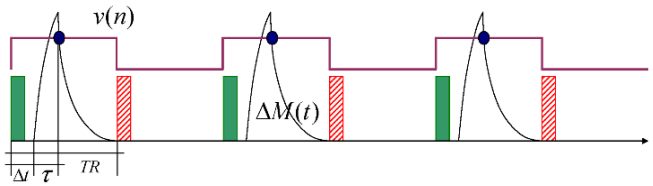

Fig. 1. Schematics of PASL labeling strategy. The rectangular signal (purple) represents $v(t)$, and its value is equal to one for labeling acquisition and zero for a non-labeling acquisition. Δt is the time delay between the labeling of the arterial blood and reaching the tissues, τ is the instant where the acquisition is made, and TR is the time period before another sequence of labeling or non labeling can occur.

The image $\mathbf{\Gamma}(t) = \{\eta_{i,j}(t)\}$ is assumed to be *Additive White Gaussian Noise* (AWGN)[16], [17] where $\eta_{ij}(t) \sim \mathcal{N}\left(0, \sigma_y^2\right)$ are stationary independent and identically distributed (iid) random variables with Gaussian distribution.

In order to simplify the problem formulation and algorithm design let us consider the following alternative formulation for the observation model described in equation (5),

$$\mathbf{Y} = \boldsymbol{f}\boldsymbol{u}^T + \mathbf{D} + \mathbf{\Delta m}\boldsymbol{v}^T + \boldsymbol{N} \quad (6)$$

where the t^{th} columns of $\mathbf{Y} = \{y_i(t)\}$, $\mathbf{D} = \{d_i(t)\}$ and $\boldsymbol{N} = \{\eta_i(t)\}$ are vectorized versions of the corresponding images, arranged by *lexicographic* order of their pixel index [18]. In practice, these image sequences, after vectorization, are arranged in $NM \times L$ matrices. The time invariant images F and ΔM, after vectorization, give rise to the $NM \times 1$ column vectors $\boldsymbol{f}$ and $\mathbf{\Delta m}$, respectively. The signal $v(t)$ is arranged in a L column vector, $\boldsymbol{v}$, and $\boldsymbol{u}$ is a constant vector of ones with the same dimension.

The probability of $\mathbf{Y}$ is a multivariate Gaussian distribution with mean $\boldsymbol{\mu} = \boldsymbol{f}\boldsymbol{u}^T + \mathbf{D} + \mathbf{\Delta m}\boldsymbol{v}^T$ and covariance diagonal matrix, $\sigma_y^2\boldsymbol{I}$, because the noise is white,

$$p(\mathbf{Y}) \sim \mathcal{N}(\boldsymbol{\mu}, \sigma_y^2\boldsymbol{I}). \quad (7)$$

The *Maximum Likelihood* (ML) estimation of the unknown images, $\boldsymbol{\theta} = \{\boldsymbol{f}, \mathbf{D}, \mathbf{\Delta m}\}$, may be formulated as follows

$$\boldsymbol{\theta} = \arg\min_{\theta} E_y(\mathbf{Y}, \boldsymbol{v}, \boldsymbol{\theta}) \quad (8)$$

where the energy function

$$\begin{aligned} E_y(\mathbf{Y},\boldsymbol{v},\boldsymbol{\theta}) &= -\log p(Y|\boldsymbol{\theta},\boldsymbol{v}) \\ &= ||\boldsymbol{f}\boldsymbol{u}^T + \mathbf{D} + \boldsymbol{\Delta}\mathbf{m}\boldsymbol{v}^T - \mathbf{Y}||^2 + C \end{aligned} \tag{9}$$

is called *Data Fidelity Term*.

The optimization task described in equation (8) is an *ill-posed* problem [19] and regularization is needed. By using the *maximum a posteriori* (MAP) criterion the regularization is introduced by the prior distribution of the parameters. In this approach, the new energy function to be minimized is $E(\mathbf{Y},\boldsymbol{v},\boldsymbol{\theta}) = -\log p(\mathbf{Y}|\boldsymbol{\theta},\boldsymbol{v})p(\boldsymbol{\theta})$ and the estimation process is formulates as follows,

$$\boldsymbol{\theta} = \arg\min_{\theta} E(\mathbf{Y},\boldsymbol{v},\boldsymbol{\theta}) \tag{10}$$

where

$$E(\mathbf{Y},\boldsymbol{v},\boldsymbol{\theta}) = E_y(\mathbf{Y},\boldsymbol{v},\boldsymbol{\theta}) + E_\theta(\boldsymbol{\theta}) \tag{11}$$

with $E_\theta(\boldsymbol{\theta}) = -\log p(\theta)$.

Since the parameters $\boldsymbol{f}$, $\mathbf{D}$ and $\boldsymbol{\Delta}\mathbf{m}$ in $\boldsymbol{\theta}$ are assumed independent the prior term can be decomposed,

$$E_\theta(\boldsymbol{\theta}) = E_f(\boldsymbol{f}) + E_{\Delta M}(\boldsymbol{\Delta}\mathbf{m}) + E_D(\mathbf{D}) \tag{12}$$

Here, the parameter images $\boldsymbol{f}$, $\mathbf{D}$ and $\boldsymbol{\Delta}\mathbf{m}$ in $\boldsymbol{\theta}$ are considered *Markov Random Fields* which means its priors are Gibbs distributions [19],

$$p(\boldsymbol{\tau}) = \frac{1}{Z_\tau} e^{-\alpha_\tau U(\boldsymbol{\tau})} \tag{13}$$

where $U(\boldsymbol{\tau})$ is called *Gibbs* energy with $\boldsymbol{\tau} \in \{\boldsymbol{f}, \mathbf{D}, \boldsymbol{\Delta}\mathbf{m}\}$ and α_τ are the prior hyper-parameters. The *Gibbs* energy for 2D images is

$$U(\boldsymbol{\tau}) = \sum_i \left(\delta_h^2(i) + \delta_v^2(i)\right) \tag{14}$$

where i is the index of each pixel of the image and $\delta_h(i)$ and $\delta_v(i)$ are the differences of the i^{th} pixel to its horizontal and vertical neighbors respectively.

In case of time varying *Drift* imaged, $\mathbf{D}$, a third term is added to account for the temporal dimension

$$U(\mathbf{D}) = \sum_{i,t} \left(\delta_h^2(i,t) + \delta_v^2(i,t) + \delta_t^2(i,t)\right) \tag{15}$$

where $\delta_t(i,t) = d_i(t) - d_i(t-1)$.

Equation (11) can be written in the matricial form:

$$\begin{aligned} E \quad & (\mathbf{Y},\boldsymbol{v},\boldsymbol{\theta}) = \\ \tfrac{1}{2} \quad & Tr[(\boldsymbol{f}\boldsymbol{u}^T + \mathbf{D} + \boldsymbol{\Delta}\mathbf{m}\boldsymbol{v}^T - \mathbf{Y})^T(\boldsymbol{f}\boldsymbol{u}^T + \mathbf{D} + \boldsymbol{\Delta}\mathbf{m}\boldsymbol{v}^T - \mathbf{Y})] + \\ \alpha_f \quad & [(\phi_h\boldsymbol{f})^T(\phi_h\boldsymbol{f}) + (\phi_v\boldsymbol{f})^T(\phi_v\boldsymbol{f})] + \\ \alpha_m \quad & [(\phi_h\boldsymbol{\Delta}\boldsymbol{m})^T(\phi_h\boldsymbol{\Delta}\boldsymbol{m}) + (\phi_v\boldsymbol{\Delta}\boldsymbol{m})^T(\phi_v\boldsymbol{\Delta}\boldsymbol{m})] + \\ \alpha_D \quad & Tr[(\phi_h\boldsymbol{D})^T(\phi_h\boldsymbol{D}) + (\phi_v\boldsymbol{D})^T(\phi_v\boldsymbol{D}) + \\ \alpha_{Dt} \quad & Tr[(\boldsymbol{D}\phi_t)(\boldsymbol{D}\phi_t)^T] \end{aligned} \tag{16}$$

where ϕ_h, ϕ_v and ϕ_t are $M \times M$, $N \times N$ and $L \times L$ matrices respectively, used to compute the horizontal and vertical first order differences. Tr stands for the trace of a matrix. Both matrices, ϕ_h and ϕ_v, have the following structure (although different dimensions)

$$\phi = \begin{pmatrix} 1 & 0 & 0 & \dots & \dots & 0 & 0 & -1 \\ -1 & 1 & 0 & \dots & \dots & \dots & 0 & 0 \\ 0 & -1 & 1 & \dots & \dots & \dots & 0 & 0 \\ \dots & \dots & \dots & \dots & \dots & -1 & 1 & 0 \\ 0 & 0 & 0 & \dots & \dots & 0 & -1 & 1 \end{pmatrix} \tag{17}$$

Equation (16) can be simplified as follows

$$\begin{aligned} E \quad & (\mathbf{Y},\boldsymbol{v},\boldsymbol{\theta}) = \\ \tfrac{1}{2} \quad & Tr[(\boldsymbol{f}\boldsymbol{u}^T + \mathbf{D} + \boldsymbol{\Delta}\mathbf{m}\boldsymbol{v}^T - \mathbf{Y})^T(\boldsymbol{f}\boldsymbol{u}^T + \mathbf{D} + \boldsymbol{\Delta}\mathbf{m}\boldsymbol{v}^T - \mathbf{Y})] + \\ & \alpha_f \boldsymbol{f}^T\Psi\boldsymbol{f} + \alpha_m\boldsymbol{\Delta}\boldsymbol{m}^T\Psi\boldsymbol{\Delta}\boldsymbol{m} + \alpha_D Tr[\boldsymbol{D}^T\Psi\boldsymbol{D}] + \alpha_{Dt}Tr[\boldsymbol{D}\Psi_t\boldsymbol{D}^T] \end{aligned} \tag{18}$$

where $\Psi = \phi_h^T\phi_h + \phi_v^T\phi_v$ and $\Psi_t = \phi_t\phi_t^T$. The minimizers of (19) are the roots of the gradients of E with respect to $\boldsymbol{f}$ and $\boldsymbol{\Delta}\boldsymbol{m}$,

$$\begin{cases} \nabla_{\mathbf{f}} E &= (\boldsymbol{f}\boldsymbol{u}^T + \mathbf{D} + \boldsymbol{\Delta}\mathbf{m}\boldsymbol{v}^T - \mathbf{Y})\boldsymbol{u} + \alpha_f\Psi^T\boldsymbol{f} = 0 \\ \nabla_{\boldsymbol{\Delta}\mathbf{m}} E &= (\boldsymbol{f}\boldsymbol{u}^T + \mathbf{D} + \boldsymbol{\Delta}\mathbf{m}\boldsymbol{v}^T - \mathbf{Y})\boldsymbol{v} + \alpha_m\Psi^T\boldsymbol{\Delta}\mathbf{m} = 0 \end{cases} \tag{19}$$

Defining the following auxiliary variables

$$\begin{aligned} \boldsymbol{A_f} &= l\boldsymbol{I} + \alpha_f\boldsymbol{\Psi}^T && (20)\\ \boldsymbol{a_f} &= (\mathbf{Y} - \mathbf{D})\boldsymbol{u} && (21)\\ a_m &= \boldsymbol{v^T u} && (22)\\ \boldsymbol{A_b} &= (\boldsymbol{v^T v})\boldsymbol{I} + \alpha_m\boldsymbol{\Psi^T} && (23)\\ \boldsymbol{a_m} &= \mathbf{Y} - \mathbf{D}\boldsymbol{v} && (24)\\ a_f &= \boldsymbol{u^T v} && (25) \end{aligned}$$

the following simplified version of (19) is obtained,

$$\begin{cases} \mathbf{A_f f} + a_m\boldsymbol{\Delta}\mathbf{m} &= \mathbf{a_f} \\ a_f\mathbf{f} + \mathbf{A_m}\boldsymbol{\Delta}\mathbf{m} &= \mathbf{a_m} \end{cases} \tag{26}$$

The solution to this system is

$$\begin{cases} \hat{\boldsymbol{\Delta}\mathbf{m}} &= (a_f a_m\boldsymbol{I} - \boldsymbol{A_f A_m})^{-1}(a_f\boldsymbol{a_f} - \boldsymbol{A_f a_b}) \\ \hat{\boldsymbol{f}} &= (a_m a_f\boldsymbol{I} - \boldsymbol{A_m A_f})^{-1}(a_m\boldsymbol{a_m} - \boldsymbol{A_m a_f}) \end{cases}$$

The stationary point of E w.r.t. $\mathbf{D}$ is computed by finding the roots of the gradient of E (see (19)) with respect to $\mathbf{D}$,

$$\nabla_{\mathbf{D}} E = (\boldsymbol{D} + \boldsymbol{f}\boldsymbol{u^T} + \boldsymbol{\Delta m v^T} - \boldsymbol{Y}) + \alpha_D\boldsymbol{\Psi^T}\mathbf{D} + \alpha_{Dt}\boldsymbol{D\Psi_t} = 0 \tag{27}$$

Defining the following auxiliary variable

$$\begin{aligned} \boldsymbol{A} &= \xi\boldsymbol{I} + \alpha_D\boldsymbol{\Psi^T} && (28)\\ \boldsymbol{B} &= ((1-\xi)\boldsymbol{I} + \alpha_{Dt}\boldsymbol{\Psi_t}) && (29)\\ \boldsymbol{C} &= -\boldsymbol{Y} - \boldsymbol{f}\boldsymbol{u^T} - \boldsymbol{\Delta m v^T} && (30) \end{aligned}$$

equation (27) can be re-written as follows

$$\boldsymbol{AD} + \boldsymbol{DB} + \boldsymbol{C} = \mathbf{0} \tag{31}$$

which is the well known *Sylvester-Lyapunov* equation, commonly used in control theory [19], [20], [21].

The equations (27) and (31) are iteratively computed until convergence is achieved.

Pair-wise and surround subtractions implementation

After having implemented the proposed algorithm, the two subtraction methods most commonly used in the literature were also adapted to the considered problem formulation for comparison. Based on (5), they were introduced as follows:

Pair-wise subtraction:

$$\mathbf{\Delta m} = \frac{\sum_{i=1,2}^{l-1} Y(i) - Y(i+1)}{l/2} \tag{32}$$

Surround subtraction:

$$\mathbf{\Delta m} = \frac{Y(1) - Y(2) + \sum_{i=3,2}^{l-1} (Y(i) - \frac{Y(i-1)+Y(i+2)}{2})}{l/2} \tag{33}$$

IV. Experimental Results and Discussion

A. Synthetic Data

Synthetic ASL data were generated based on a test object with structure similar to the human brain: one axial slice of a real brain mask, segmented into two main regions, *White Matter*(WM) and *Gray Matter*(GM) was used, as shown in Figure 2. The relative perfusion intensity of each region was defined for each experiment as described in the following.

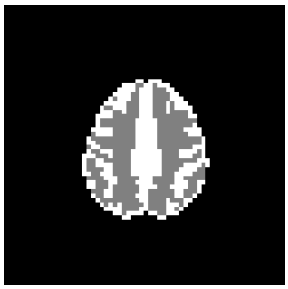

Fig. 2. Synthetic data test object, derived from a real brain mask (64×64 matrix size). The two different regions, colored in white and gray, represent the white and gray matter of the human brain.

Simulation Parameters

As a first step towards the validation of the proposed algorithm, all the parameters of the bayesian algorithm were set to 0. The value of the noise (σ) was set to 1, which adds AWGN with mean value and standard deviation equal to 1, and the magnetization difference ($\mathbf{\Delta M}$) was set to 1 for the GM and 0.5 for the WM. This represents a noise intensity similar to the intensity of the signal, as expected in the real case (mentioned in Chapter 1). The drift signal ($\mathbf{D}$) is a slow-varying cosine, between -1 and 1, and the background intensity of the image ($\mathbf{F}$) is 10000. These parameters were kept unaltered throughout the tests, with the exception of the noise level. In Figure 3, it is presented an image representation of a control acquisition and a labeled acquisition, after the addition of the noise.

In Figure 3 the labeling is not visible in the acquired image, as it tends to disappear in the noise corrupting the image.

Having simulated the acquisition of 50 labeled images and 50 controls, the vector of images was processed with the 3 methods, and the results are shown in Figure 4.

The quantitative assessment of the proposed algorithm performance was expressed in terms of *Improved SNR*(dB) (ISNR) and Mean Error(%) (ME). The ISNR is obtained by subtracting the SNR of the image acquired pre-processing

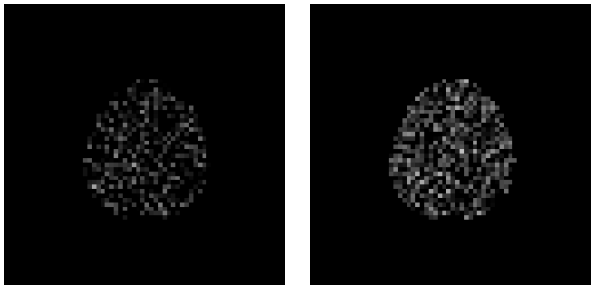

Fig. 3. A control (left) and a labeling acquisition (right) using synthetic data.

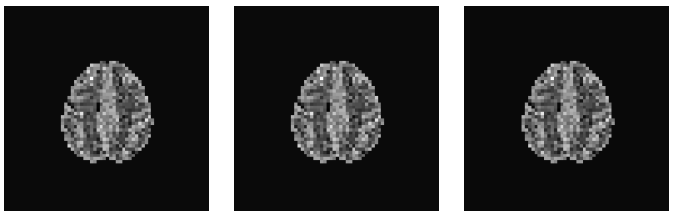

Fig. 4. Images obtained with the three signal processing methods: proposed algorithm, with priors equal to zero (left), pair-wise subtraction (center) and surround subtraction (right).

(SNR_i) to the value of the SNR obtained post-processing (SNR_f), $ISNR = SNR_f - SNR_i$ (dB). The SNR of the pre and post-processing images is calculated as shown in equation (34),

$$SNR = \left(\frac{A_{signal}}{A_{noise}}\right)^2 \tag{34}$$

where A_{signal} and A_{noise} are the amplitude of the signal and noise, respectively. On the other hand, the value of the ME of the estimated image is calculated according to equation (35)

$$ME(\%) = \frac{100}{N \times M} \sum_{i=1,j=1}^{N,M} \frac{|\hat{x}_{i,j} - x_{i,j}|}{x_{i,j}} \tag{35}$$

where N and M are the dimensions of columns and rows of the matrix image, and $\hat{\mathbf{X}}$ and $\mathbf{X}$ the estimation and the original labeling images, accordingly.

The results obtained in this first experiment are given in Table II and in Figure 5. These are the mean values of the results obtained for ISNR and ME in 200 simulations, performed under the same conditions.

TABLE II
Mean values of ISNR and ME for the test realized with all priors equal to zero.

Method	ISNR (dB)	Mean error (%)
Proposed algorithm	13.906	24.658
Pair-wise subtraction	13.906	24.658
Surround subtraction	13.999	24.393

By comparing the values of Table II, it is clear that in the absence of prior, the proposed algorithm performs exactly like the pair-wise subtraction.

Moreover, surround subtraction performs slightly better, presenting higher ISNR and lower ME. This result was ex-

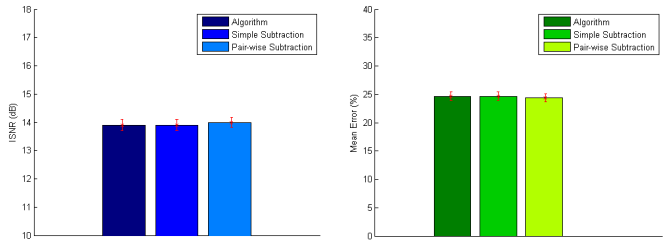

Fig. 5. Graphical comparison of the values of *ISNR* and *ME* obtained using each of the 3 methods: bars represent the mean and error bars represent the standard deviation.

pected, considering that this approach copes best with slow varying drift.

Prior optimization

The search for the optimal priors to be used in the upcoming tests was performed on a trial-error basis. Considering equation (16), the only priors that are directly related to the image estimation are β and γ (α is related to the drift signal), therefore only these two were optimized.

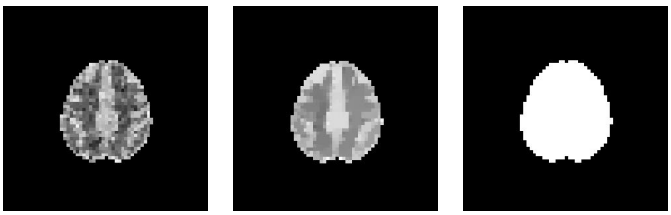

Fig. 6. Images obtained with different sets of priors. From left to right, less to more rigid imposition.

The selection of the value for the prior is a very delicate process. By choosing a small value, the algorithm might not have sufficient "strength" to pull the solution towards an optimal value and considering an excessively large value, the force pulling towards the solution can cause over-smoothing, as shown in Figure 6.

The choice of the optimal value was performed with a dual criteria, which consisted in the selection of the set of parameters that provided higher ISNR, associated with lower ME.

A series of 200 simulations were performed for every set of different values of the priors varying from 0 to 10. For values greater than 10, the prior over-smoothed the resulting image, hence these were not considered. The mean results are presented in Figure 7.

Evaluating the graphics, it is clear that higher SNR values come from manipulating the value of γ, the prior for ΔM. Among the options, it was selected the value that presented the higher ISNR but at the same time did not compromise the ME of the image. The value of $\gamma = 5$ was selected from the results depicted in Figure 8, which shows the evaluation of both parameters of interest, with respect to increasing prior value.

All the remaining priors values were set to 1.

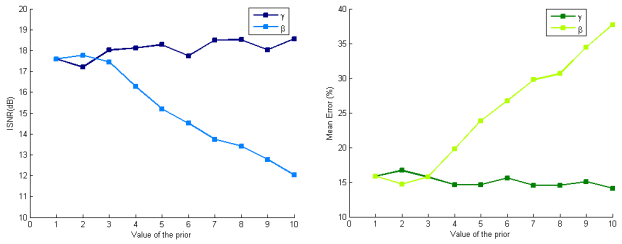

Fig. 7. In the first graphic, the value of ISNR with ascending values of β and γ. In the second graphic, the corresponding ME.

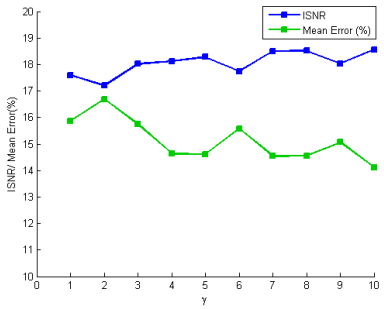

Fig. 8. Evolution of the values of ISNR and ME of the estimated image with increasing value of γ.

With the chosen values, the proposed algorithm was then tested (200 simulations) against the two subtraction methods and the results are displayed in Figure 9

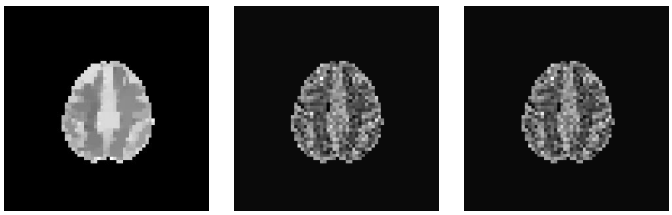

Fig. 9. Images obtained with the proposed algorithm using the optimized prior (left), pair-wise subtraction (middle) and surround subtraction (right).

In this Figure, it is evident the reduction of the noise corrupting the image. Image areas with the same intensity are more homogeneous in the image obtained with the algorithm than those produced by the common subtraction methods. The edges remain visible and easier to identify. Figure 10 represent a spatial perspective of the results and a linear cut through the diagonal of the image, respectively.

The spikes from the image obtained with the algorithm were reduced as a result of the prior pulling towards an optimal solution.

The mean values of ISNR and ME for this test are given in Table III.

TABLE III
MEAN VALUES OF ISNR AND ME FOR THE TEST REALIZED WITH THE OPTIMIZED PRIOR.

Method	ISNR (dB)	Mean error (%)
Proposed algorithm	16.990	17.807
Pair-wise subtraction	14.026	24.492
Surround subtraction	14.103	24.269

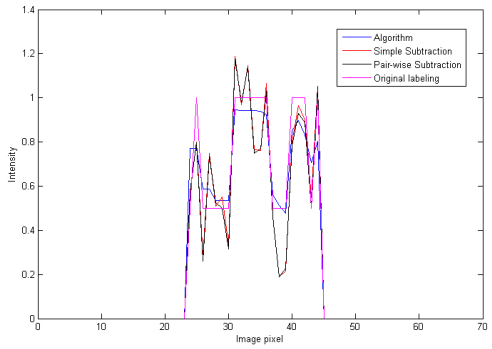

Fig. 10. Image profile through the diagonal of the estimated image.

In this case, the proposed algorithm obtained an higher value of SNR, approximately $3dB$, and reduced the overall ME by 7%. These values represent an improvement of 23% on SNR and a reduction of ME in aproximately 30%, which expresses an increase of almost one quarter of the total value for the SNR and over a quarter for the redution of ME. The results of Table III were introduced into a bar graphic, Figure 11, for better analysis.

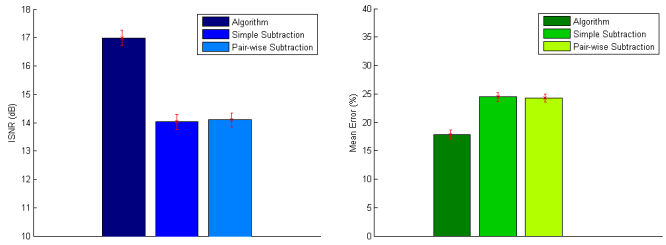

Fig. 11. Graphical comparison for the values of *ISNR* and *ME* obtained for the 3 methods - prior established situation.

The previous test was the closest approximation to the real case, in which all the parameters replicate the values of the physiological parameters. To study the performance in different noise levels, a series of Monte Carlo simulations (500 for each noise level) were performed. The mean results are shown in Figure 12.

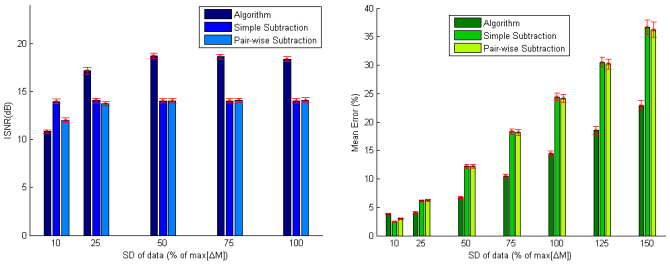

Fig. 12. Value of ISNR and ME for the three methods, as function of $\%$ of noise.

For noise levels of 10% of the signal intensity, the traditional subtraction methods performed slightly better than the bayesian algorithm. However, as the noise sistematically increases, the proposed algorithm fastly outperformed the traditional approaches, and at levels of 25%, already the bayesian approach becomes a major advantage. With increasing values of noise, the value of the SNR tends to stabilize, in opposition to the overal ME, which grows systematically, although at a lower rate than for the data driven models.

B. Real Data

After testing the proposed algorithm in a set of synthetic data, a set of real acquired images was considered. The real data were acquired from on healthy subject, on a 3T Siemens MRI system (Hospital da Luz, Lisboa) using a PICORE-Q2TIPS PASL sequence[22], with the following parameters: TI1/TI1s/TI2 = 750ms/900ms/1700ms; GE-EPI readout with TR/TE = 2500ms/19ms; 201 repetitions; 9 contiguous axial slices positioned parallel to the AC-PC line, with spatial resolution of 3.5 $\times$ 3.5 $\times$ 7.0 mm^3 and matrix size 64 $\times$ 64 $\times$ 9.

Some modifications had to be performed to the proposed algorithm in order to enable the manipulation of these real data, namely the customization of horizontal and vertical difference matrices from equation (17) for each slice of the data (the algorithm is only applied to pixels containing relevant data information, thus excluding all the pixels outside the brain region). Due to the fact that the stopping criteria is no longer available for real data, since one cannot calculate the ME of the estimation with respect to the real value of every pixel in the real data case, the algorithm underwent another transformation, as the stopping criteria became the number of cycle iterations, manually imposed.

Having successfully implemented these alterations, the algorithm was then tested, with the same prior values obtained from the results of synthetic data. Since with the real data set not all the necessary information for the use of the equations (34) and (35) is available, the results are discussed in a qualitative manner.

Unprocessed control and labeled images are depicted in Figure 13.

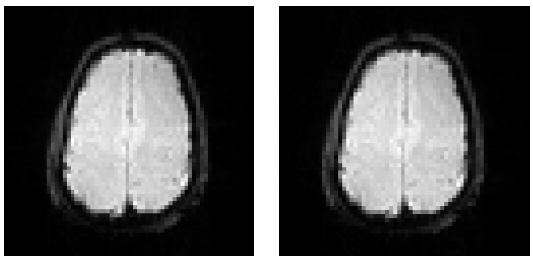

Fig. 13. Images of a control (left) and labeled (right) acquisitions of one brain slice, acquired from a healthy subject using a PASL sequence on a 3T MRI system.

The first results obtained are depicted in Figure 14 and were obtained with 200 iterations of the proposed algorithm. They are compared with the images obtained by pair-wise subtraction and surround subtraction.

Analyzing Figure 14, the image obtained with the proposed algorithm presents less noise corruption and better distinction of different brain details. Nevertheless, seeking further image improvement, a sequence of tests with different iteration values

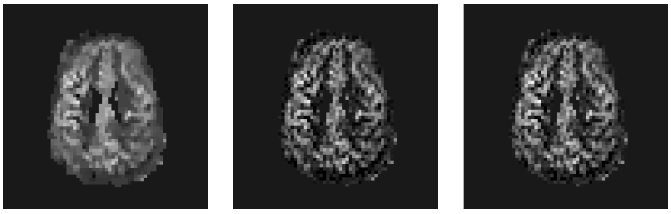

Fig. 14. Images obtained with the proposed algorithm (optimized prior, 200 iterations) (left), pair-wise subtraction (center) and surround subtraction (right).

was then performed. The results obtained are shown in Figure 15.

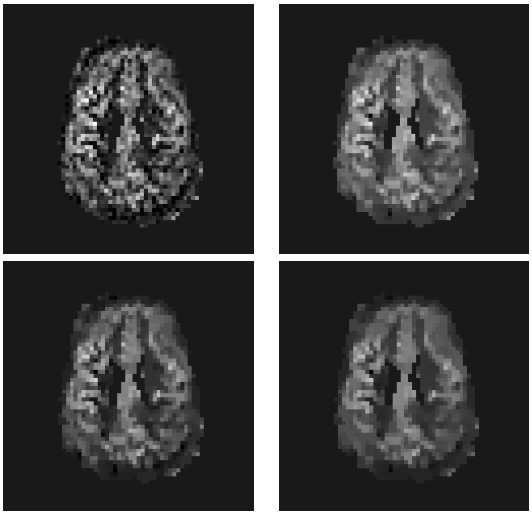

Fig. 15. Processed images obtained with increasing number of iterations (50, 100, 200 and 400 iterations), from left to right and top to bottom.

The noise removal and image smoothing is observable in Figure 15 with increasing iteration number used in the proposed algorithm, and with no compromise of the image edges and transitions.

In Figures 16 and 17 a comparison of the images resulting from the proposed algorithm, using the optimized prior and number of iterations, and the previously mentioned signal processing methods is shown.

Fig. 16. Images obtained with the proposed algorithm (optimized prior, 400 iterations) (left), pair-wise subtraction (center) and surround subtraction (right).

Figure 16 displays the resulting improved image quality obtained with the algorithm. The enhancement was obtained at some computational expense, since a larger number of iterations results in a longer processing time. Nevertheless, the purpose of medical imaging is to provide accurate anatomical

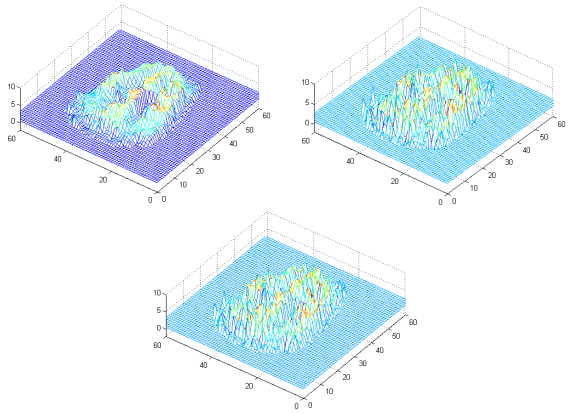

Fig. 17. A spatial view of images obtained with the proposed algorithm(400 iterations), pair-wise and surround subtraction, respectively.

or functional images and this computational cost is a small disadvantage when compared to the possible advantages that emerge from this new approach.

V. Conclusion

Arterial Spin Labeling imaging is a technique to which is recognized great potential, since it can provide useful information about an important physiological parameter, *perfusion*. When comparing ASL to the other perfusion measuring techniques, its main advantages are the non-invasiveness and repeatability, while its main disadvantage is the low intrinsic SNR. In the medical field, as in many others, it is of high interest to obtain the best images possible, and this is the foundation of this thesis. The main objective was to implement a signal processing model to cope with the low SNR of the images produced, as well as improving the overall mean error of the estimation. Currently, ASL images are obtained by subtracting the control and the labeled images, with no further considerations, therefore, considered a data driven approach. The processing method proposed in this thesis incorporates *a priori* knowledge onto the estimation equation, hence improving the quality of the image reconstruction. This *a priori* knowledge is the assumption that no drastic variations of signal along the same tissue are expected, except at the organs boundaries, where signal variations are likely to be intense.

The image estimation problem was formulated in a *bayesian* framework, and after some careful mathematical considerations, the proposed algorithm was implemented and tested on synthetic data. The results obtained, as described in Section IV-A, show great improvement in image SNR, approximately 23% increase compared to pair-wise subtraction, as well as a decrease of around 30% in the overall mean error of the estimation, hence fulfilling the objectives initially proposed.

Having determined empirically the optimal prior values with synthetic data, and encouraged by the results obtained, the algorithm was further tested with a set of real data. These images are depicted in Section IV-B, and present less noise corruption, as the smoother shape and sharp frontiers suggest.

Although good results were achieved, the current work

opens many possibilities for future work, and some are suggested in the following section.

Future Work

To improve even further image processing or explore the possibilities, some points of particular interest may be approach in future research:

- Automatic prior calculation
  Instead of empirically choosing the numerical value to assign to the priors, on a trial and error basis, the algorithm could be reformulated in order to calculate, on each iteration, the optimal value of the prior.
- Reducing the number of control acquisitions
  One of the major set-backs of ASL is the long duration of the acquisition. For every labeling, a control image is also acquired, in order to minimize the influences of signal fluctuations. However, by decreasing the number of control acquisitions, without compromising image quality, the acquisition time could be reduced. One of the properties of the algorithm proposed is that it also accounts for the presence of temporal drift, hence reducing the need of the label-control sequence for attenuation of this effect.
  For this purpose, testing with sequences other than the strict alternate labeling-control approach could be a mean for reducing acquisition times.
- Validation tests on empirical data
  Further performance analysis on real data sets is necessary in order to achieve the algorithm validation. In particular, it would be of interest to test the performance of the proposed algorithm in terms of the intra- and inter-subject reproducibility of the perfusion estimates, compared to the most common subtraction methodologies.

REFERENCES

[1] T.T. Liu and G.G. Brown. Measurement of cerebral perfusion with arterial spin labeling: Part 1. Methods. *Journal of the International Neuropsychological Society*, 13(03):517–525, 2007.

[2] F. Calamante, D.L. Thomas, G.S. Pell, J. Wiersma, and R. Turner. Measuring cerebral blood flow using magnetic resonance imaging techniques. *Journal of cerebral blood flow & metabolism*, 19(7):701–735, 1999.

[3] J.A. Detre. Arterial spin labeled perfusion mri. *Clinical Neurology*, 2008.

[4] J.A. Detre and D.C. Alsop. Perfusion magnetic resonance imaging with continuous arterial spin labeling: methods and clinical applications in the central nervous system. *European journal of radiology*, 30(2):115–124, 1999.

[5] J.M. Pollock, H. Tan, R.A. Kraft, C.T. Whitlow, J.H. Burdette, and J.A. Maldjian. Arterial Spin Labeled MRI Perfusion Imaging: Clinical Applications. *Magnetic resonance imaging clinics of North America*, 17(2):315, 2009.

[6] R.B. Buxton, L.R. Frank, E.C. Wong, B. Siewert, S. Warach, and R.R. Edelman. A general kinetic model for quantitative perfusion imaging with arterial spin labeling. *Magnetic resonance in medicine*, 40(3):383–396, 1998.

[7] D.S. Williams, J.A. Detre, J.S. Leigh, and A.P. Koretsky. Magnetic resonance imaging of perfusion using spin inversion of arterial water. *Proceedings of the National Academy of Sciences*, 89(1):212, 1992.

[8] ET Petersen, I. Zimine, Y.C.L. Ho, and X. Golay. Non-invasive measurement of perfusion: a critical review of arterial spin labelling techniques. *British journal of radiology*, 79(944):688, 2006.

[9] R.R. Edelman, D.G. Darby, and S. Warach. Qualitative mapping of cerebral blood flow and functional localization with echo-planar mr imaging and signal targeting with alternating radio frequency. *Radiology*, 192:513–520, 1994.

[10] DM Garcia, C. De Bazelaire, and D. Alsop. Pseudo-continuous flow driven adiabatic inversion for arterial spin labeling. In *Proc Int Soc Magn Reson Med*, volume 13, page 37, 2005.

[11] W.C. Wu, M. Fernández-Seara, J.A. Detre, F.W. Wehrli, and J. Wang. A theoretical and experimental investigation of the tagging efficiency of pseudocontinuous arterial spin labeling. *Magnetic Resonance in Medicine*, 58(5):1020–1027, 2007.

[12] E.C. Wong, M. Cronin, W.C. Wu, B. Inglis, L.R. Frank, and T.T. Liu. Velocity-selective arterial spin labeling. *Magnetic Resonance in Medicine*, 55:1334–1341, 2006.

[13] T.T. Liu and E.C. Wonga. A signal processing model for arterial spin labeling functional MRI. *NeuroImage*, 24:207–215, 2005.

[14] GK Aguirre, JA Detre, E. Zarahn, and DC Alsop. Experimental Design and the Relative Sensitivity of BOLD and Perfusion fMRI. *NeuroImage*, 15:488–500, 2002.

[15] E.C. Wong, R.B. Buxton, and L.R. Frank. Implementation of Quantitative Perfusion Imaging Techniques for Functional Brain Mapping using Pulsed Arterial Spin Labeling. *NMR in Biomedicine*, 10:237–249, 1997.

[16] P. Bao and L. Zhang. Noise reduction for magnetic resonance images via adaptive multiscale products thresholding. *Medical Imaging, IEEE Transactions on*, 22(9):1089–1099, 2003.

[17] ME Alexander, R. Baumgartner, AR Summers, C. Windischberger, M. Klarhoefer, E. Moser, and RL Somorjai. A wavelet-based method for improving signal-to-noise ratio and contrast in MR images. *Magnetic Resonance Imaging*, 18(2):169–180, 2000.

[18] T.K. Moon and W.C. Stirling. *Mathematical methods and algorithms for signal processing*, volume 13. Prentice hall New York, 2000.

[19] J.M. Sanches, J.C. Nascimento, and J.S. Marques. Medical image noise reduction using the Sylvester–Lyapunov equation. *IEEE transactions on image processing*, 17(9), 2008.

[20] V. Balakrishnan and E. Feron. Linear matrix inequalities in control theory and applications. *International Journal of Robust and Nonlinear Control*, 6(9/10):896–1099, 1996.

[21] E.T. Petersen, T. Lim, and X. Golay. Model-free arterial spin labeling quantification approach for perfusion MRI. *Magnetic Resonance in Medicine*, 55(2):219–232, 2006.

[22] W.M. Luh, E.C. Wong, P.A. Bandettini, J.S. Hyde, et al. Quipss ii with thin-slice ti 1 periodic saturation: a method for improving accuracy of quantitative perfusion imaging using pulsed arterial spin labeling. *Magnetic resonance in medicine*, 41(6):1246–1254, 1999.